ACS NANO

Subscriber access provided by Princeton University Library

Article

Bending Properties of Single Functionalized Graphene Sheets Probed by Atomic Force Microscopy

Hannes C. Schniepp, Konstantin N. Kudin, Je-Luen Li, Robert K. Prud'homme, Roberto Car, Dudley A. Saville, and Ilhan A. Aksay

ACS Nano, **2008**, 2 (12), 2577-2584 • DOI: 10.1021/nn800457s • Publication Date (Web): 10 December 2008

Downloaded from http://pubs.acs.org on December 31, 2008

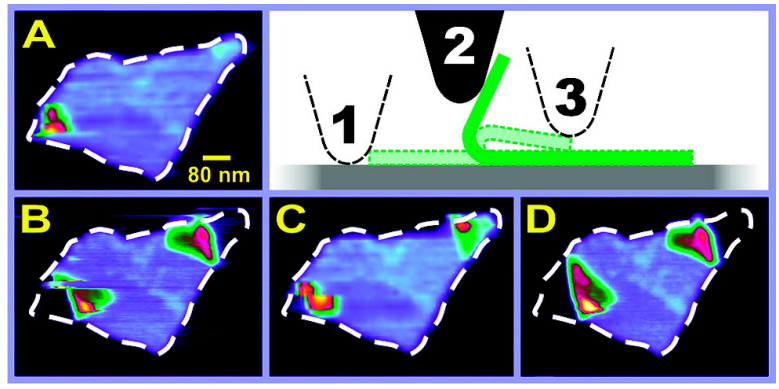

More About This Article

Additional resources and features associated with this article are available within the HTML version:

- Supporting Information
- Access to high resolution figures
- Links to articles and content related to this article
- Copyright permission to reproduce figures and/or text from this article

View the Full Text HTML

ACS Publications
High quality. High impact.

ACS Nano is published by the American Chemical Society. 1155 Sixteenth Street N.W., Washington, DC 20036

Bending Properties of Single Functionalized Graphene Sheets Probed by Atomic Force Microscopy

Hannes C. Schniepp,[†,§] Konstantin N. Kudin,[‡] Je-Luen Li,[‡,∥] Robert K. Prud'homme,[†] Roberto Car,[‡] Dudley A. Saville,[†,¶] and Ilhan A. Aksay[†,*]

[†]Department of Chemical Engineering, and [‡]Department of Chemistry, Princeton University, Princeton, New Jersey 08544. [§]Current address: The College of William and Mary, Department of Applied Science, Williamsburg, VA 23185. [∥]Current address: Institute of Atomic and Molecular Sciences, Academia Sinica, Taipei, Taiwan. [¶]Deceased.

ABSTRACT We probe the bending characteristics of functionalized graphene sheets with the tip of an atomic force microscope. Individual sheets are transformed from a flat into a folded configuration. Sheets can be reversibly folded and unfolded multiple times, and the folding always occurs at the same location. This observation suggests that the folding and bending behavior of the sheets is dominated by pre-existing kink (or even fault) lines consisting of defects and/or functional groups.

KEYWORDS: graphene · nanocomposites · mechanical properties · bending modulus · atomic force microscopy · density functional theory

Graphene possesses unique mechanical[1−6] and electronic[1−3,7−21] properties. Recently, a near-complete exfoliation of bulk amounts of graphite into single functionalized graphene sheets has been demonstrated by two complementary methods.[22−26] In both methods, the first and a common step is the oxidation of graphite to graphite oxide.[27,28] In one process, graphite oxide is expanded and reduced thermally[22,23,29] to yield single functionalized graphene sheets (FGSs). In the other, graphite oxide is split into single graphene oxide sheets by ultrasonication and then reduced chemically.[24−26] In both cases, the resultant materials are different than perfect graphene sheets due to the retention of some of the graphene oxide characteristics and the presence of defects. However, nanocomposites based on these materials have become viable and offer the great promise of translating some of the unique properties of graphene into engineering materials.[5,25,30−34] In contrast to the traditional composites based on carbon, these nanocomposites provide dramatically improved thermal, mechanical, and electrical properties at very low loadings of the nanofiller component.[25,30] We are interested in understanding and improving the mechanical properties of these composites. These mechanical properties depend on (i) the dispersion of the nanofiller in the polymer matrix, (ii) the mechanical properties of the matrix−filler interface, and (iii) the mechanical properties of the filler itself. In particular, our interest here is on understanding the role of the defect structure of FGS on its bending characteristics as the bending characteristics play an important role in the low strain regime of the composites. The load transfer from a matrix to the reinforcement filler at low strains will be dominated by the bending behavior of the filler rather than its in-plane modulus before the graphene sheets are fully flattened.

The FGSs are significantly different from pristine graphene, as they bear epoxy, hydroxyl, and carboxyl side groups attached to the graphitic backbone,[35] and lattice defects that are generated during the thermal reduction step.[22,26,29] During the thermal exfoliation and reduction of graphite oxide, the material is strongly reduced, leaving the final C/O ratio at about 12/1−22/1. Since most of the material escaping at this stage is CO_2, we conclude that the carbon backbone acquires defects.[22,23,29] The sheets typically are of several hundred nanometers in diameter and feature linear wrinkles and a higher surface roughness than pristine graphene due to the presence of functional groups and defects.[22] For high-resolution structural characterization of the sheets by atomic force microscope (AFM), we apply tapping mode where lateral forces exerted by the tip are negligible so that the sheets remain unaltered. A typical tapping-mode AFM image of several

*Address correspondence to iaksay@princeton.edu.

Received for review July 21, 2008 and accepted November 11, 2008.

Published online December 10, 2008. 10.1021/nn800457s CCC: $40.75

© 2008 American Chemical Society

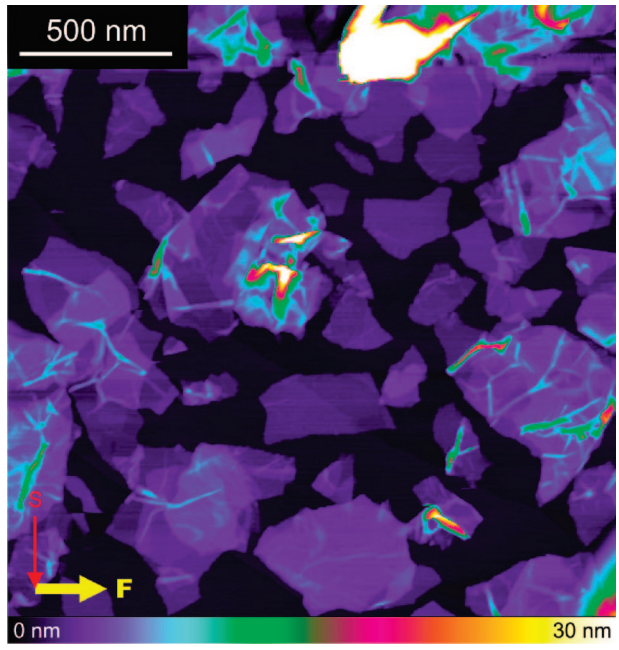

Figure 1. AFM imaging of functionalized graphene sheets. Tapping-mode image showing the wrinkled structure of many of the sheets.

FGSs located on top of a substrate of highly oriented pyrolytic graphite (HOPG) is shown in Figure 1.

We have demonstrated earlier that fault lines containing functional groups or defects can lead to kinks in the sheets.[22,36] One important type of defect in graphene is the 5−8−5 defect, which has lower energy on the curved graphitic surfaces[37] and thus can give rise to curvature in graphene.[22] This curvature becomes evident when the equilibrium structures of the sheets containing such defects are determined computationally. The example shown in Figure 2 was determined using periodic boundary conditions. Figure 2a shows 2 × 2 unit cells in planar view. In order to comply with the periodic boundary conditions, any overall curvature of the sheet needs to be avoided. Therefore, the two defects, "1" and "2", have been introduced into the unit cell with opposite orientations, such that one defect compensates for the curvature of the other. The curvature induced by the two defects can be seen in the side view (Figure 2b): the sheet has significant local curvature along the lines of subsequent 5−8−5 defects (colored in light cyan and light yellow, in the direction of the green unit vector). We suggest such defect lines as one possible origin of the observed wrinkles in FGSs. In this work, we use AFM to study and manipulate these wrinkled sheets experimentally in order to understand the role of the defect lines on the bending properties of the sheets. Our results are complemented by computational modeling on the mechanical behavior of kinked sheets.

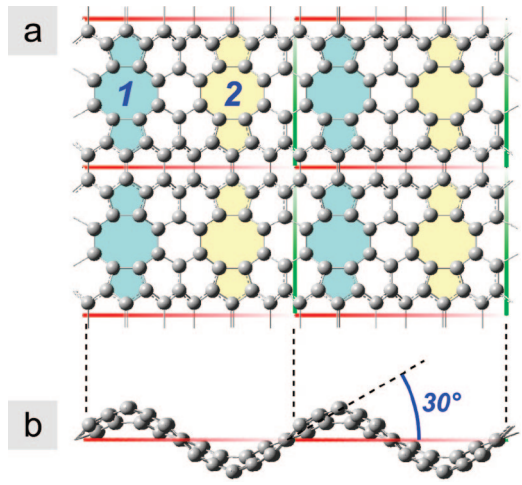

Figure 2. Pattern of 5−8−5 defects in graphene organized in linear fashion. (a) Top view of 2 × 2 unit cells with two defects, each. (b) Side view shows that the two defect lines introduce kinks in the sheet. The defects are organized such that the bending of defects "1" (light cyan) is compensated by the bending of defects "2" (light yellow), so that a flat sheet results.

RESULTS AND DISCUSSION

In the following sections, we first present our AFM observations on the flexural conformation of the FGSs and show that in many cases bending occurs at the same site. We then provide a theoretical approach based on first-principle calculations that supports some of our experimental findings.

Manipulation of FGSs by AFM. The lateral forces exerted by the tip on the sample in contact-mode AFM imaging are substantial. In our experiments, we use a set point corresponding to a vertical force of 1 nN, which resulted in lateral forces on the order of 50 nN measured by monitoring the cantilever torsion. These forces are capable of inducing structural modifications in the imaged samples, which lead to sudden changes in the observed topography and the cantilever force signals during imaging. As previously demonstrated for carbon nanotubes (CNT),[38,39] we analyze these signals to reconstruct the manipulation events and to study the mechanical characteristics of the FGS on the sample surface. The two most common types of such tip-induced manipulation are moving (Figure 3a) and folding (Figure 3b). For the correct interpretation of these images, we recall the sequential nature of AFM imaging: the horizontal scan lines not only represent different positions of the sample but also different times during the scanning process. If the sheet location or conformation changes during image acquisition, all lines acquired before the event reflect the old constellation, and all lines acquired after this event show the new state. We thus recognize such manipulation events as sudden changes between two subsequent horizontal scan lines. In Figure 3a, the white arrow points to the area where the AFM tip first contacts the sheet. After imaging the sheet for a few scan lines, a discontinuity occurs, indicated by a green arrow. After the discontinuity, the left and right edges of the sheet are shifted toward the right, indicating that the sheet was moved on the surface. In

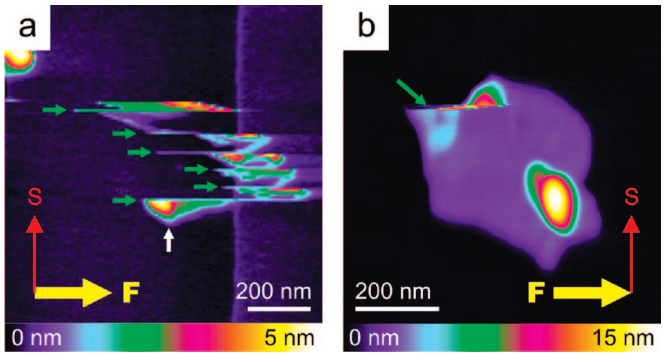

Figure 3. FGS modification through AFM. (a) Image of a sheet that was moved by the AFM probe in one contact-mode scan several times (moving events highlighted by green arrows). (b) During a contact-mode scan, the sheet got folded by the AFM probe (position indicated by green arrow). Yellow and red arrows: fast and slow scanning directions, respectively.

the remainder of the image, there are five more such events where the sheet is moved to the left and finally out of the scanning area without being completely imaged. Note that the substrate itself stays in place, as the vertical dark blue line in the right half of the image—representing a step in the HOPG substrate—is continuous. A folding event of an FGS is shown in Figure 3b. In contrast to Figure 3a, only a small part at the top right (indicated by the green arrow) of the sheet is actually moved to the right. The right edge of the same sheet remains continuous in the lines where the event occurs, proving that the sheet is not moved on the surface.

Determining the FGS Conformation. Figure 4 shows a sequence of four contact-mode AFM images of exactly the same sample area, featuring one and the same FGS at different stages of folding. In Figure 4a, the sheet is almost completely flat; panels b−d in Figure 4 depict the progressing folding process. The white, dashed line—the footprint of (a) manually overlaid in panels (a) to (d)—shows how the sheet area becomes more and more reduced in the left and right corners. Next to the "missing" areas, the sheets feature an increased topography. The fact that the missing areas and these areas with increased topography behave like mirror images further supports our claim that we have folded the sheet, as illustrated in Figure 4e. Two folding events at the left sheet edge are visible in Figure 4b,c, each highlighted by a green arrow.

Quantitative analysis of the topography data confirms this scenario. Figure 5a shows a topography cross-section following the yellow, dotted line in Figure 4d. The cross-section leads across the two folded areas, highlighted in purple and wine. These areas are higher due to the second, folded layer of FGS. In the center of the curve, where only one layer is present, the average height is 1.44 nm, within the expected range for an individual FGS.[22] The way we picture the folded areas is shown in Figure 5b. The second layer folded on top (orange) is assumed to be as flat as the first layer that is in contact with the substrate. The actual bending occurs in a limited area (blue) that includes the highest part of the cross-section. The total bending angle in the blue area is about 180°. Further away from the bending area, the top layer touches the first layer (green). The peak heights in the measured cross-sections close to the left and right edges of the folded areas are 4 and 5 nm, respectively—more than twice as much as the height of the unfolded first layer. This indicates that there is a small gap between the upper and the lower layers of the sheet close to the bending area due to the flexural rigidity of the sheet, as suggested in Figure 5b). To calculate the radius of curvature r of the graphitic backbone of the folded sheets in the bending area, we have to consider that the sheet thickness of ~1.5 nm also contributes to the measured height of the folded sheets of ~4.5 nm. Considering this correction, we find $r = (4.5\ \text{nm} - 1.5\ \text{nm})/2 = 1.5\ \text{nm}$.

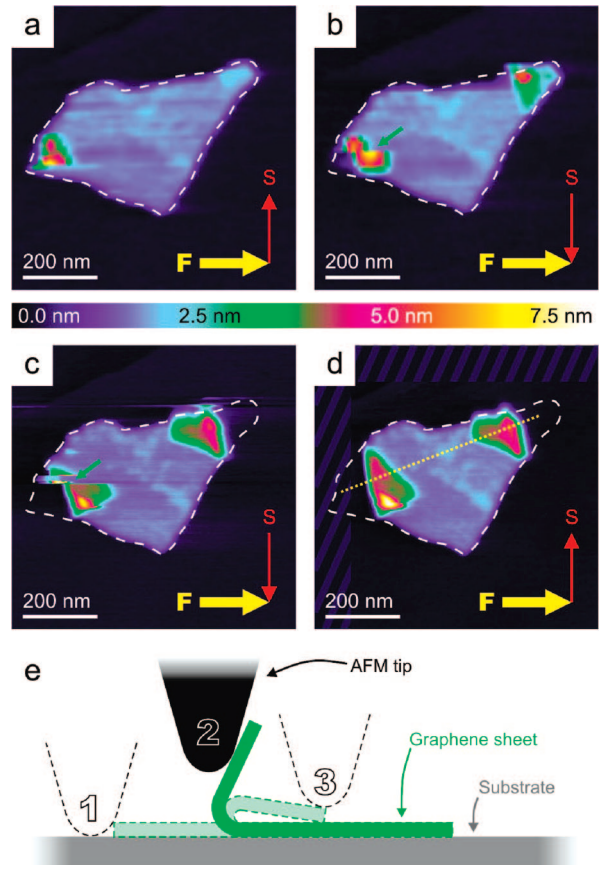

Figure 4. Folding a functionalized graphene sheet by contact-mode AFM. (a) The sheet is in almost completely flat conformation. (b) The top right and bottom left edges are partially folded by the AFM probe. (c) Folding progresses. (d) The folded sheet reaches a stable conformation. The hatched area was not part of the actual scan but added later to make comparison with (a)−(c) easier. The green arrows in (b) and (c) indicate lines in which folding events occurred. (e) Illustration of the folding process: (1) the tip first lifts a part of the sheet (green) off the substrate (gray). (2) The sheet is bent until it touches itself (3).

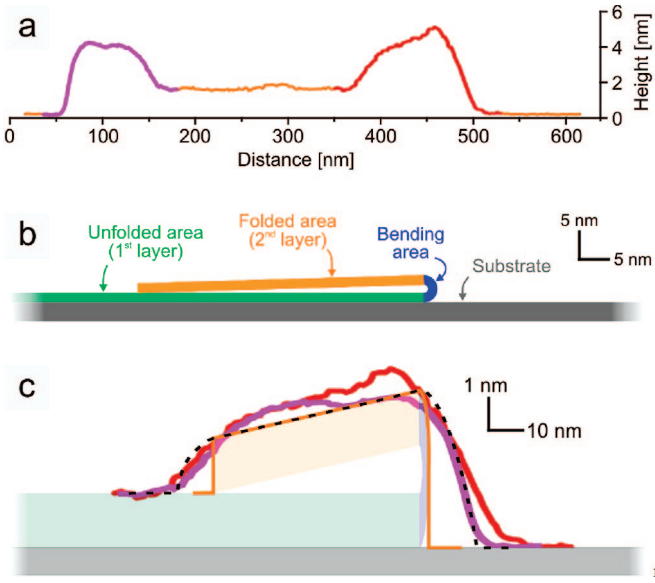

Figure 5. Topology of a folded sheet: (a) Cross-section through the sheet shown in Figure 4d (vertical scale about 20 times magnified with respect to the horizontal scale). (b) Division of folded sheet into zones. (c) Measured sections across edges of folded sheet (purple and wine lines, from (a)) shown on top of the idealized, folded sheet from (b) (in background faint colors) at a 10-fold magnified vertical scale. Black dotted line: simulated AFM cross-section of the sheet in background, considering the shape of the AFM probe.

In Figure 5c, the folded model sheet of Figure 5b is displayed with a 10-fold magnified vertical scale (in faint colors in the background) to facilitate a comparison with the AFM data (overlaid in purple and burgundy). The solid, orange line would be obtained as cross-section if this model sheet were imaged with an infinitely sharp, perfect AFM probe. The dotted, black curve is the simulated topography[40] of the model sheet taking into account an AFM tip with a 20 nm radius of curvature. This simulated curve is in very good agreement with the overlaid topography data measured at the two folded areas. For future studies, it would be interesting to vary the force set point to test whether changing the applied vertical force has an effect on the number of folding events and on the obtained folding geometries.

In our picture of the folded FGSs, attractive van der Waals (vdW) forces between the first and the second layer of the folded sheet counter the restoring forces of the bending area. When these attractive forces are stronger than the restoring forces due to bending, the sheet stays in a folded conformation, akin to the collapse of a CNT.[41,42] For collapsed CNTs, it was shown that a quantitative analysis of the balance between these forces can be carried out.[41,42] We set out to perform a similar calculation for FGS. If the attractive forces are known, we can, in principle, estimate the flexural rigidity of FGS. We calculated the attractive forces based on the measured topography of folded sheets. From the measured height of folded sheets as a function of position, we estimated the local separation between the folded layers. The total attractive force between the two opposing layers of a folded sheet was then calculated adding up the contributions of all pairs of points in the two layers. Our calculations, however, yielded too large error bars to make meaningful statements about the bending stiffness of FGS. Most likely, this is due to the lack of information on the atomic-scale structure of FGS. The separations between the atoms in the two layers, which influence the van der Waals interactions very critically, can thus not be determined with good enough accuracy. More details on our methods and results are summarized in the Supporting Information.

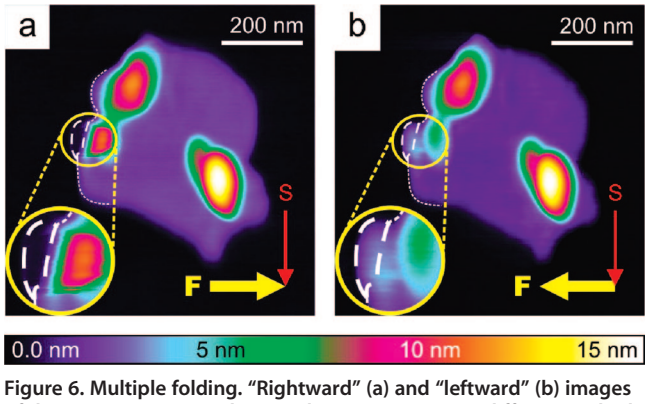

Figure 6. Multiple folding. "Rightward" (a) and "leftward" (b) images of the same contact-mode scan showing systematic differences (highlighted area in circles) due to folding and unfolding of the sheet in every scan line.

Multiple, Reversible Folding. Not in all cases the tip-induced folding of FGS resulted in a stable conformation of the FGSs. For several FGSs, we have evidence that they were folded back and forth by the AFM probe many times along the same bending lines. To demonstrate this, we compare the "rightward" and "leftward" images of the same AFM scan (Figure 6a,b). The images are essentially identical, except the area highlighted by the yellow circle. The rightward image (Figure 6a) has a smaller footprint than the leftward image (Figure 6b); the corresponding region is bordered by a white, dashed line in both images. On the area to the right of the missing footprint, the topography is higher than in the corresponding area in Figure 6b, suggesting that Figure 6a shows a folded version of the sheet in Figure 6b. Interestingly, both images were taken virtually at the same time: Figure 6a is composed of scan lines where the probe was scanned from left to right; Figure 6b shows the data acquired in the scan lines where the tip returned to the left. In the area inside the yellow circle, the sheet conformation was hence changed in every single scan line: when the tip was moved from left to right, the edge appeared folded and on the way back unfolded. In other words, depending on the scanning direction, the sheet is either found in state "3" or "1" of the folding process described in Figure 4e, and this folding line was in the same place during all measurements. This observation allows two different pos-

sible scenarios: (i) unstable folding, and (ii) reversible folding. In both cases, the sheet is folded (1→3) during the rightward tip motion. Either the sheet immediately flips back once the tip leaves and stops holding it in position 3 ("unstable folding", (i)) or the sheet first stays in position 3 but is transferred back 3→1 when the tip crosses it in reverse direction ("reversible folding", (ii)). An immediate question then is why is the folding occurring always at the same line? In the section below, we relate the folding sites to the presence of defect lines.

Modeling of the Mechanical Properties of FGS. The mechanical properties of the individual sheets are expected to differ from pristine graphene due to (i) the addition of functional surface groups, (ii) the creation of defects during the reduction process, and (iii) resulting topological modifications of the FGSs, such as wrinkling and buckling. To investigate issues (i) and (ii) rigorously, it would be pivotal to know the atomic-scale structure of the FGS. This information is not yet available. However, we can make some general considerations. Adding functional groups to the graphitic backbone alone should not dramatically change the mechanical properties at the atomic level since the strength of most covalent bonds is relatively similar.[43] Similarly, it has been shown that defects in CNTs, while having a significant impact on the ultimate strength, do not have a substantial influence on the stiffness at small defect concentrations.[44] The mechanical loading we induce in FGS in this work with the AFM tip is moderate; we do not observe failure of the material. In this regime, the mechanical behavior of the material is determined by its stiffness rather than by its strength. Consequently, we do not expect a dramatic influence on the mechanical properties of the FGSs coming directly from (i) functional groups or (ii) defects. Instead, we focus on (iii) the effects of wrinkling on the mechanical properties of graphene sheets as discussed below.

In the folding of FGSs that we observe experimentally, there is a balance between the mechanical restoring forces and the vdW interactions. While the former can be described with high accuracy using the density functional theory (DFT), vdW interactions cannot be treated using the same approach. To study the bending energetics of kinked graphene, we closed kinked pieces of graphene to tubes. This way, no vdW forces are necessary to counter the mechanical restoring forces of the bent sheets. Also, the number of atoms in this configuration is relatively small so that DFT calculations can be carried out. The calculations were done using a (20,20) CNT precursor (80 carbon atoms in the unit cell) that was repeated infinitely along the tube axis (periodic boundary conditions). The radius of curvature of a (20,20) CNT is about 1.2 nm, similar to the curvature we observe in the geometries of the folded sheets. A segment with five repeat units is shown in Figure 7a. We introduced two kink lines parallel to the tube axis. Rather than selecting a certain chemistry or

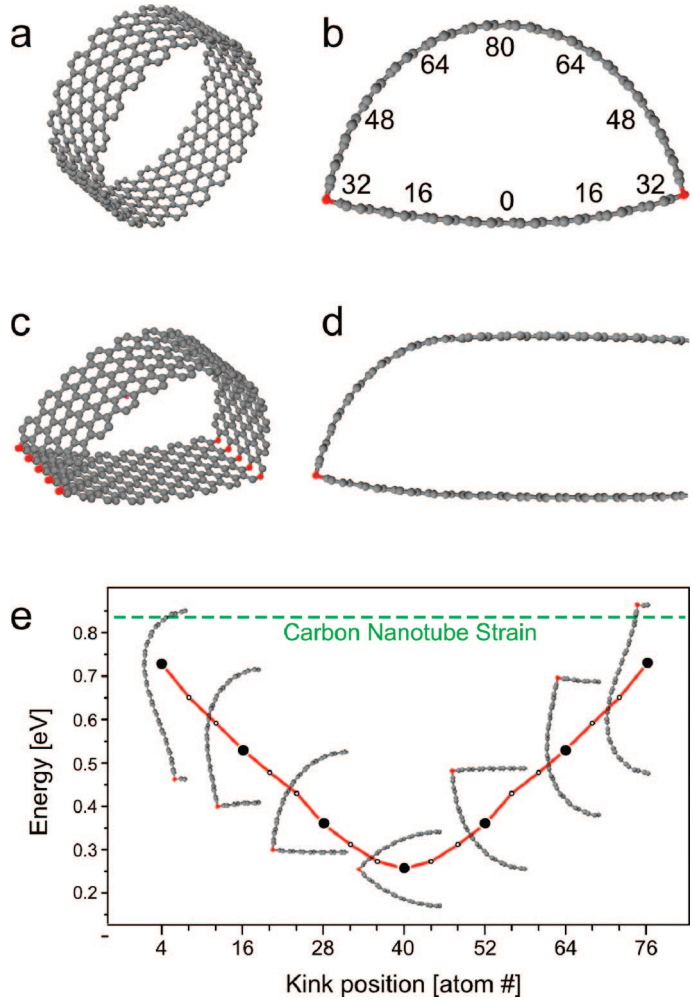

Figure 7. Bending of graphene with a pre-existing fault line. (a) Five repeat units of an 80 atom, pristine CNT unit cell (no kink). (b) Calculated cross-section through a tube with two 90° kinks introduced. (c) Side view, showing the repeated structure. (d) Side view of a folded sheet equivalent to the scenario shown in (b). (e) Energy of the tube as a function of position of the kink lines with respect to the corresponding flat, relaxed structure.

molecular structure for the kinks—such as the 5−8−5 defects we suggested to be responsible for the wrinkles—we simply forced two bond angles in the ring to be 90° (the choice of 90° is arbitrary). This procedure avoids the introduction of any chemistry-specific behavior. Also, the unit cell is kept relatively small, reducing the computation time. An example is shown in Figure 7b,c (cross-section and five repeat units, respectively); the atoms with kinked bonds are colored red. As far as the flexural strain is concerned, one-half of the tube with two kinks in Figure 7b is equivalent to a kinked sheet with one kink as illustrated in Figure 7d. We performed a series of calculations in which one kink was kept in the same place, while the relative position of the second kink in the ring was varied between atoms 4 and 76 (position numbers indicated in Figure 7b). The strain energies of these structures were determined by calculating their total energy and subtract-

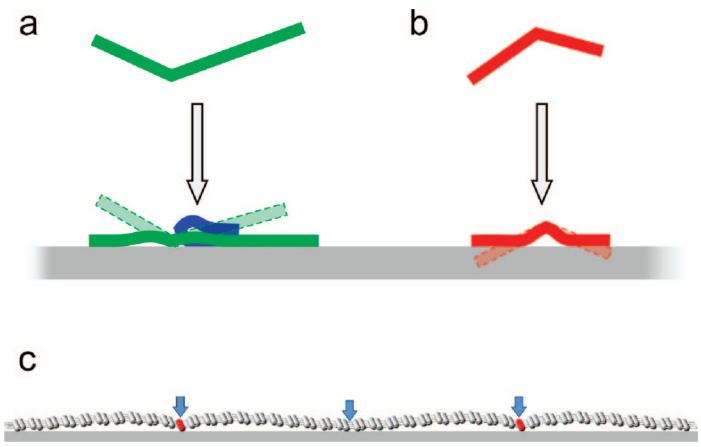

Figure 8. Adsorption and folding of wrinkled sheets. Depending on the orientation of a sheet on the surface, a wrinkle can either adsorb with the sharp (a) or the blunt (b) side on the surface. (c) Simulation of a sheet facing the substrate with the sharp side. The atoms highlighted by blue arrows were constrained to the substrate plane.

ing the energy of the corresponding unbent structures. The results are compared to the strain energy of the perfect CNT with the same number of atoms (Figure 7a). The results are plotted as a function of the kink position in Figure 7e. All strain energies are significantly lower than the strain energy of a pristine CNT (shown in green), demonstrating that the existing fault lines should facilitate bending or folding of such sheets at a lower energy cost, supporting the experimental observations presented above. The strain energy is maximal when the defect lines are positioned close to one of the two extreme positions 0 and 80; the energy reaches a minimum for the symmetrical center position 40. A selection of the corresponding equilibrium structures is superimposed on the plot. The most energetically favorable folded configuration is achieved when the kinks are located symmetrically at the apexes (position 40 in Figure 7b). Accordingly, we can conclude that folding a sheet with a pre-existing kink is energetically favorable over folding a perfectly flat sheet. Moreover, the lowest energy of such folding will be achieved when the kink is exactly in the middle of the folding line. Thus, our calculations show that existing kink lines in an FGS will facilitate folding. This can explain our experimental observation that some sheets can be folded back and forth exactly at the same position, several times. Thus, we suggest that there are existing defect lines that are located at these preferred folding sites. According to our previous studies, such defect lines may be caused by the formation of 5−8−5 defects produced from the reduction of epoxide lines.[22,36]

Interactions of FGS with the Substrate. Our conclusion that the folding occurs along pre-existing kink lines is deduced indirectly, based on the mechanical behavior of the sheets. It may seem surprising that our AFM data do not show any evidence of such defect lines prior to folding. In the following, we show that the fault lines having the proper orientation for folding are systematically not visible in our data.

For our AFM investigations, the sheets need to be supported by a substrate. When the sheets adsorb on the substrate from the dispersion during sample preparation, each kink in the sheets faces the substrate either with the sharp or with the blunt side, as indicated in Figure 8a,b, respectively. However, only in the former configuration of the fault line can the sheet be folded into a low-energy configuration corresponding to Figure 7d,e. In the latter configuration, this is impossible due to the presence of the substrate. While the kinks in the former configuration (Figure 8a) give rise to negative topographic features ("dips"), the latter scenario (Figure 8b) induces a positive topographic feature ("bump"). In our experimental evidence consisting of hundreds of AFM images similar to Figure 1, we see a myriad of examples for the latter scenario, but not a single case exhibiting a topography corresponding to the former. Thus, the kinks that are in the orientation that can be folded by the AFM tip into a low-energy state (Figure 8a) are *all* invisible in our AFM images, whereas the visible wrinkles *all* correspond to configuration shown in Figure 8b, which cannot be folded.

We performed further numerical simulations to support this explanation more quantitatively. Since the substrate−sheet vdW attractions could not easily be included into our DFT calculations, we mimicked them by taking a kinked sheet and forcing certain atoms to be in contact with the substrate using external constraints (atoms highlighted by the blue arrows in Figure 8c). Our results confirm that the sheet only features a minimal topography modulation of a couple of angstroms under these conditions (Figure 8c depicts the resulting relaxed structure). This is not enough contrast to be easily visualized by AFM on the rough sheets. Future experiments with higher resolution imaging (for instance using scanning tunneling microscopy) may provide further clarification.

CONCLUSIONS

By performing in-depth analysis of the AFM data, we have shown evidence for tip-induced conformational changes of the functionalized graphene sheets. We have demonstrated transformation of sheets into folded states, which are stable, most likely through attractive vdW forces. In some cases, we see that sheets fold back and forth at exactly the same position multiple times. This suggests that the sheets have certain areas at which folding is more favorable than in others. We suggest that the wrinkles present in the FGSs may pose such preferred bending sites. Using DFT-based calculations, we support this idea and demonstrate that folding of sheets with pre-existing kink lines is energetically favored over folding of unwrinkled sheets. Moreover, in the folded conformation with the lowest

energy, the kink line is located in the apex of the wrinkle. This is in agreement with our experimental observation where folding a sheet repeatedly occurs at exactly the same position.

METHODS

Sample Preparation. For sample preparation, 5.5 mg of FGSs (production described in ref 22 and Supporting Information thereof) and 3.0 mL of 1-methyl-2-pyrrolidinone (NMP) were placed in an 8 mL scintillation vial containing a magnetic stir bar. The vial was immersed in an ice bath, while the suspension was ultrasonicated (VirSonic 100, The Virtis Co., Gardiner, NY) with an output power of 12 W for 5 min under continuous stirring. After allowing the suspension to sit at room temperature for 1 h, an aliquot (0.5 mL) was taken and added to a 1.5 mL flex tube for centrifugation. The samples were centrifuged for nine cycles at 10 000 RPM for 5 min each. The sedimented material was discarded after each cycle, finally yielding a light-brown suspension. The suspension was spin-coated at 5 000 RPM onto freshly cleaved HOPG substrates.

Atomic Force Microscopy. The samples were examined using a MultiMode/NanoScope IIIa AFM (Veeco Metrology LLC, Santa Barbara, CA) in contact and tapping modes. For contact mode, Veeco NP-S type tips were used (oxide-sharpened and gold-coated silicon nitride cantilevers with nominal force constant $k = 0.32$ N/m and radius of curvature $r = 20$ nm). For tapping mode, Veeco MP 11100 silicon cantilevers were used (resonance frequency $f = 300$ kHz, $k = 40$ N/m, $r < 10$ nm). The AFM images were flattened[45] to compensate for drifts and piezo creep. In all images, the slow scanning axis is vertical; the actual direction of the slow scanning axis—"upward" or "downward"—is indicated by a red arrow with the letter "S" in each image. Correspondingly, the direction of the fast scanning direction—"leftward" or "rightward"—is indicated by horizontal, yellow arrows with the letter "F".

Calculations. The calculations in this work were carried out *via* an implementation of DFT with Gaussian-type orbitals and periodic boundary conditions (PBC)[46] available in Gaussian03.[47] We employed the gradient corrected Perdew, Burke, Ernzerhof (PBE)[48] together with the double-ζ quality 3-21G Gaussian basis set.[49] Full geometry optimizations were carried out *via* a redundant internal coordinate method[50] for periodic systems,[51] where the lattice vectors are optimized implicitly *via* a combination of intercell bonds, valence angles, and dihedrals. In the cases with some constrained coordinates, the constraints were specified *via* the standard approach provided by the redundant internal coordinate optimization method.[50]

Acknowledgment. Financial support from the National Science Foundation NIRT under Grant No. CMS-0609049 and the NASA University Research, Engineering, and Technology Institute on BioInspired Materials (BIMat) under Award No. NCC-1-02037 is greatly appreciated.

Supporting Information Available: Information on our analysis of the balance between attractive and restoring forces in the folded sheets are available. This material is available free of charge *via* the Internet at http://pubs.acs.org.

REFERENCES AND NOTES

1. Kelly, B. T. *Physics of Graphite*; Applied Science: London, 1981.
2. Bernholc, J.; Brenner, D. W.; Buongiorno Nardelli, M.; Meunier, V.; Roland, C. Mechanical and Electrical Properties of Nanotubes. *Annu. Rev. Mater. Res.* **2002**, *32*, 347–375.
3. Gomez-Navarro, C.; Burghard, M.; Kern, K. Elastic Properties of Chemically Derived Single Graphene Sheets. *Nano Lett.* **2008**, *8*, 2045–2049.
4. Bunch, J. S.; van der Zande, A. M.; Verbridge, S. S.; Frank, I. W.; Tanenbaum, D. M.; Parpia, J. M.; Craighead, H. G.; McEuen, P. L. Electromechanical Resonators from Graphene Sheets. *Science* **2007**, *315*, 490–493.
5. Ramanathan, T.; Abdala, A. A.; Stankovich, S.; Dikin, D. A.; Herrera-Alonso, M.; Piner, R. D.; Adamson, D. H.; Schniepp, H. C.; Ruoff, R. S.; Nguyen, S. T.; *et al.* Functionalized Graphene Sheets for Polymer Nanocomposites. *Nat. Nanotechnol.* **2008**, *3*, 327–331.
6. Lee, C.; Wei, X.; Kysar, J. W.; Hone, J. Measurement of the Elastic Properties and Intrinsic Strength of Monolayer Graphene. *Science* **2008**, *321*, 385–388.
7. Duplock, E. J.; Scheffler, M.; Lindan, P. J. D. Hallmark of Perfect Graphene. *Phys. Rev. Lett.* **2004**, *92*, 225502-1–225502-4.
8. Novoselov, K. S.; Geim, A. K.; Mozorov, S. V.; Jiang, D.; Zhang, Y.; Dubonos, S. V.; Grigorieva, I. V.; Firsov, A. A. Electric Field Effect in Atomically Thin Carbon Films. *Science* **2004**, *306*, 666–669.
9. Novoselov, K. S.; Geim, A. K.; Morozov, S. V.; Jiang, D.; Katsnelson, M. I.; Grigorieva, I. V.; Dubonos, S. V.; Firsov, A. A. Two-Dimensional Gas of Massless Dirac Fermions in Graphene. *Nature* **2005**, *438*, 197–200.
10. Novoselov, K. S.; Jiang, D.; Schedin, F.; Booth, T. J.; Khotkevich, V. V.; Morozov, S. V.; Geim, A. K. Two-Dimensional Atomic Crystals. *Proc. Natl. Acad. Sci. U.S.A.* **2005**, *102*, 10451–10453.
11. Novoselov, K. S.; McCann, E.; Morozov, S. V.; Fal'ko, V. I.; Katsnelson, M. I.; Zeitler, U.; Jiang, D.; Schedin, F.; Geim, A. K. Unconventional Quantum Hall Effect and Berry's Phase of 2 pi In Bilayer Graphene. *Nat. Phys.* **2006**, *2*, 177–180.
12. Zhang, Y.; Tan, Y.-W.; Stormer, H. L.; Kim, P. Experimental Observation of the Quantum Hall Effect and Berry's Phase in Graphene. *Nature* **2005**, *438*, 201–204.
13. Gusynin, V. P.; Sharapov, S. G. Unconventional Integer Quantum Hall Effect in Graphene. *Phys. Rev. Lett.* **2005**, *95*, 146801-1–146801-4.
14. Wilson, M. Electrons in Atomically Thin Carbon Sheets Behave Like Massless Particles. *Phys. Today* **2006**, *59*, 21–23.
15. McCann, E.; Fal'ko, V. I. Landau-Level Degeneracy and Quantum Hall Effect in a Graphite Bilayer. *Phys. Rev. Lett.* **2006**, *96*, 086805-1–086805-4.
16. Peres, N. M. R.; Guinea, F.; Neto, A. H. C. Electronic Properties of Disordered Two-Dimensional Carbon. *Phys. Rev. B* **2006**, *73*, 125411-1–125411-23.
17. Berger, C.; Song, Z. M.; Li, X. B.; Wu, X. S.; Brown, N.; Naud, C.; Mayo, D.; Li, T. B.; Hass, J.; Marchenkov, A. N.; *et al.* Electronic Confinement and Coherence in Patterned Epitaxial Graphene. *Science* **2006**, *312*, 1191–1196.
18. Katsnelson, M. I.; Novoselov, K. S.; Geim, A. K. Chiral Tunnelling and the Klein Paradox in Graphene. *Nat. Phys.* **2006**, *2*, 620–625.
19. Geim, A. K.; Novoselov, K. S. The Rise of Graphene. *Nat. Mater.* **2007**, *6*, 183–191.
20. Meyer, J. C.; Geim, A. K.; Katsnelson, M. I.; Novoselov, K. S.; Booth, T. J.; Roth, S. The Structure of Suspended Graphene Sheets. *Nature* **2007**, *446*, 60–63.
21. Eda, G.; Fanchini, G.; Chowalla, M. Large-Area Ultrathin Films of Reduced Graphene Oxide as a Transparent and Flexible Electronic Material. *Nat. Nanotechnol.* **2008**, *3*, 270–274.
22. Schniepp, H. C.; Li, J.-L.; McAllister, M. J.; Sai, H.; Herrera-Alonso, M.; Adamson, D. H.; Prud'homme, R. K.; Car, R.; Saville, D. A.; Aksay, I. A. Functionalized Single Graphene Sheets Derived from Splitting Graphite Oxide. *J. Phys. Chem. B* **2006**, *110*, 8535–8539.
23. McAllister, M.; Li, J.-L.; Adamson, D. H.; Schniepp, H. C.; Abdala, A. A.; Liu, J.; Herrera-Alonso, M.; Milius, D. L.; Car, R.; Prud'homme, R. K.; *et al. Chem. Mater.* **2007**, *19*, 4396–4404.

24. Stankovich, S.; Piner, R. D.; Chen, X.; Wu, N.; Nguyen, S. T.; Ruoff, R. S. Stable Aqueous Dispersions of Graphitic Nanoplatelets via the Reduction of Exfoliated Graphite Oxide in the Presence of Poly (Sodium 4-Styrenesulfonate). *J. Mater. Chem.* **2006**, *16*, 155–158.
25. Stankovich, S.; Dikin, D. A.; Dommett, G. H. B.; Kohlhaas, K. M.; Zimney, E. J.; Stach, E. A.; Piner, R. D.; Nguyen, S. T.; Ruoff, R. S. Graphene-Based Composite Materials. *Nature* **2006**, *442*, 282–286.
26. Stankovich, S.; Piner, R. D.; Nguyen, S. T.; Ruoff, R. S. Synthesis and Exfoliation of Isocyanate-Treated Graphene Oxide Nanoplatelets. *Carbon* **2006**, *44*, 3342–3347.
27. Staudenmaier, L. Verfahren zur Darstellung der Graphitsäure. *Ber. Dtsch. Chem. Ges.* **1898**, *31*, 1481–1487.
28. Hummers, W. S.; Offeman, R. E. Preparation of Graphite Oxide. *J. Am. Chem. Soc.* **1958**, *80*, 1339.
29. Kudin, K. N.; Ozbas, B.; Schniepp, H. C.; Prud'homme, R. K.; Aksay, I. A.; Car, R. Raman Spectra of Graphite Oxide and Functionalized Graphene Sheets. *Nano Lett.* **2008**, *8*, 36–41.
30. Dikin, D. A.; Stankovich, S.; Zimney, E. J.; Piner, R. D.; Dommett, G. H. B.; Evmenenko, G.; Nguyen, S. T.; Ruoff, R. S. Preparation and Characterization of Graphene Oxide Paper. *Nature* **2007**, *448*, 457–460.
31. Watcharotone, S.; Dikin, D. A.; Stankovich, S.; Piner, R.; Jung, I.; Dommett, G. H. B.; Evmenenko, G.; Wu, S. E.; Chen, S. F.; Liu, C. P.; *et al.* Graphene−Silica Composite Thin Films as Transparent Conductors. *Nano Lett.* **2007**, *7*, 1888–1892.
32. Muszynski, R.; Seger, B.; Kamat, P. V. Decorating Graphene Sheets with Gold Nanoparticles. *J. Phys. Chem. C* **2008**, *112*, 5263–5266.
33. Verdejo, R.; Barroso-Bujans, F.; Rodriguez-Perez, M. A.; de Saja, J. A.; Lopez-Manchado, M. A. Functionalized Graphene Sheet Filled Silicone Foam Nanocomposites. *J. Mater. Chem.* **2008**, *18*, 2221–2226.
34. Kim, H.; Macosko, C. W. Morphology and Properties of Polyester/Exfoliated Graphite Nanocomposites. *Macromolecules* **2008**, *41*, 3317–3327.
35. Lerf, A.; He, H.; Forster, M.; Klinowski, J. Structure of Graphite Oxide Revisited. *J. Phys. Chem. B* **1998**, *102*, 4477–4482.
36. Li, J.-L.; Kudin, K. N.; McAllister, M.; Prud'homme, R. K.; Aksay, I. A.; Car, R. Oxygen-Driven Unzipping of Graphitic Materials. *Phys. Rev. Lett.* **2006**, *96*, 176101-1–176101-4.
37. Amorim, R. G.; Fazzio, A.; Antonelli, A.; Novaes, F. D.; da Silva, A. J. R. Divacancies in Graphene and Carbon Nanotubes. *Nano Lett.* **2007**, *7*, 2459–2462.
38. Falvo, M. R.; Clary, G. J.; Taylor, R. M., II; Chi, V.; Brooks, F. P., Jr.; Washburn, S.; Superfine, R. Bending and Buckling of Carbon Nanotubes Under Large Strain. *Nature* **1997**, *389*, 582–584.
39. Wong, E. W.; Sheedan, P. E.; Lieber, C. M. Nanobeam Mechanics: Elasticity, Strength, and Toughness of Nanorods and Nanotubes. *Science* **1997**, *277*, 1971–1975.
40. The dotted, black curve describes the trajectory of the bottom-most point of a sphere with a radius of 20 nm that is "rolled" across the sheet.
41. Chopra, N. G.; Benedict, L. X.; Crespi, V. H.; Cohen, M. L.; Louie, S. G.; Zettl, A. Fully Collapsed Carbon Nanotubes. *Nature* **1995**, *377*, 135–138.
42. Benedict, L. X.; Chopra, N. G.; Cohen, M. L.; Zettl, A.; Louie, S. G.; Crespi, V. H. Microscopic Determination of the Interlayer Binding Energy in Graphite. *Chem. Phys. Lett.* **1998**, *286*, 490–496.
43. Kudin, K. N.; Scuseria, G. E.; Yakobson, B. I. C_2F, BN, and C Nanoshell Elasticity from *Ab Initio* Computations. *Phys. Rev. B* **2001**, *64*, 235406-1–235406-10.
44. Dumitrica, T.; Hua, M.; Yakobson, B. I. Symmetry-, Time-, and Temperature-Dependent Strength of Carbon Nanotubes. *Proc. Natl. Acad. Sci. U.S.A.* **2005**, *103*, 6105–6109.
45. *Command Reference Manual, Software Version 5.12 r3*; Digital Instruments: Santa Barbara, CA, 2000.
46. Kudin, K. N.; Scuseria, G. E. Linear-Scaling Density-Functional Theory with Gaussian Orbitals and Periodic Boundary Conditions: Efficient Evaluation of Energy and Forces *via* the Fast Multipole Method. *Phys. Rev. B* **2000**, *61*, 16440–16453.
47. http://www.gaussian.com/citation_g03.htm.
48. (a) Perdew, J. P.; Burke, K.; Ernzerhof, M. Generalized Gradient Approximation Made Simple. *Phys. Rev. Lett.* **1996**, *77*, 3865–3868. (b) Perdew, J. P.; Burke, K.; Ernzerhof, M. Erratum. *Phys. Rev. Lett.* **1996**, *78*, 1396.
49. Binkley, J. S.; Pople, J. A.; Hehre, W. J. Self-Consistent Molecular Orbital Methods. 21. Small Split-Valence Basis Sets for First-Row Elements. *J. Am. Chem. Soc.* **1980**, *102*, 939–947.
50. Peng, C. Y.; Ayala, P. Y.; Schlegl, H. B.; Frisch, M. J. Using Redundant Internal Coordinates to Optimize Equilibrium Geometries and Transition States. *J. Comput. Phys.* **1996**, *17*, 49–56.
51. Kudin, K. N.; Scuseria, G. E.; Schlegl, H. B. A Redundant Internal Coordinate Algorithm for Optimization of Periodic Systems. *J. Chem. Phys.* **2001**, *114*, 2919–2923.